High-resolution structures of the SARS-CoV-2 N7-methyltransferase inform therapeutic development

Jithesh Kottur ✉, Olga Rechkoblit, Richard Quintana-Feliciano, Daniela Sciaky and Aneel K. Aggarwal ✉

Emergence of SARS-CoV-2 coronavirus has led to millions of deaths globally. We present three high-resolution crystal structures of the SARS-CoV-2 nsp14 N7-methyltransferase core bound to S-adenosylmethionine (1.62 Å), S-adenosylhomocysteine (1.55 Å) and sinefungin (1.41 Å). We identify features of the methyltransferase core that are crucial for the development of antivirals and show SAH as the best scaffold for the design of antivirals against SARS-CoV-2 and other pathogenic coronaviruses.

The SARS-CoV-2 mRNA is capped at the 5′-end by methyltransferases (MTases) nsp14 and nsp16 (ref. [1]). Nsp14 methylates the N7 atom of guanosine to generate the $^{N7Me}GpppA_{2'OH}$-RNA structure, which is then methylated at the 2′O atom of the initiating nucleotide by nsp16 to make the $^{N7Me}GpppN_{2'OMe}$-RNA structure[1]. Both nsp14 and nsp16 use S-adenosylmethionine (SAM) as the methyl donor and generate S-adenosylhomocysteine (SAH) as the reaction byproduct. Nsp14 harbors an exoribonuclease domain (ExoN) at the N-terminus and the N7-MTase domain at the C-terminus (Fig. 1a)[2–4]. The nsp14 N7-MTase is an attractive target for the development of antivirals, but most structure-guided efforts thus far have depended on crystal structures of nsp14/nsp10 from SARS-CoV[5,6], solved to 3.2–3.4 Å resolution[2]. Although the SARS-CoV-2 nsp14/nsp10 has been imaged by cryo-EM, the resolution of these structures is limited to 2.5–3.9 Å and they do not capture interactions with SAM, SAH or sinefungin (SFG)[7,8]. We employ here fusion protein-assisted crystallization[9,10] and report high-resolution crystal structures of the nsp14 N7-MTase-TELSAM fusion (TEL-MTase; Fig. 1b) in complex with SAM, SAH and SFG (Supplementary Table 1).

The MTase core in the three structures is nearly identical, superimposing with root-mean-square deviations (RMSDs) between 0.085 and 0.09 Å for 187 Cα atoms, showing it to be essentially invariant when bound to SAM, SAH or SFG (Fig. 1c). The MTase core consists of an atypical Rossmann fold, composed of a central five stranded β-sheet (β1′, β2′, β3′, β4′ and β8′) instead of the seven stranded β-sheet (β1–β7) typically associated with class I MTases[11], including those from most viruses. Helices α1′, α2′, α3′ and αC, β-strands βA and βB, and a Zn^{2+} coordinated substructure are located on one side of the β-sheet, and two short helices αA and αB on the other (Fig. 1b). SAM, SAH and SFG are located at the C-terminal ends of strands β1′, β2′ and β3′, and are cradled by loops between β1′ and β2′, β2′ and αA, and β3′ and β4′ (Fig. 2a–c).

In the full-length nsp14 structures[2,7,8], a characteristic of the MTase fold is a 'hinge' region composed of a three-stranded β-sheet (β5′, β6′ and β7′; residues 402–433) and an interdomain loop (residues 288–299) that precedes the MTase core (Extended Data Fig. 1a–c). The β-sheet extends from the MTase core and interacts with the ExoN domain, and flexibility of the hinge has been suggested to allow for the movement between the MTase core and the ExoN domain[12]. Intriguingly, this β-sheet is disordered in our three structures, suggesting that its interactions with the ExoN domain are required for its folding and stability (Extended Data Fig. 1a). Excluding the hinge region, the SARS-CoV-2 and SARS-CoV nsp14 N7-MTase cores superimpose with a RMSD of 0.67 Å for 183 Cα atoms. The most notable difference is in residues 467–482, which fold into helix αC and β-strand βB in SARS-CoV-2 nsp14 (Extended Data Fig. 1d).

The adenine base of SAM, SAH and SFG is ensconced in a cavity formed by the Ala353, Phe367, Tyr368, Cys387 and Val389 side chains, while the N1 and N6 atoms make hydrogen bonds with the backbone amide and carboxyl groups of Tyr368, respectively, and the N3 atom makes a hydrogen bond with the amide group of Ala353 (Fig. 2a–c). The ribose sugar makes direct hydrogen bonds with the Asp352 side chain, as well as water-mediated interactions with both the Gln354 side chain and main chain. Asp352 is conserved in coronaviruses and its mutation to alanine in SARS-CoV has been shown to abrogate N7-MTase activity[2,3,13]. The tail portion is fixed by numerous interactions, including direct hydrogen bonds with the Arg310 side chain and the Gly333 and Trp385 main chain atoms, as well as intricate water-mediated interactions with Gln313, Asp331 and Asn386 side chains and the Ile332 and Trp385 main chains (Fig. 2a–c). In addition, the Pro335 ring is involved in van der Waals contacts with the nonpolar portion (atoms Cβ and Cγ) of SAM/SAH/SFG. Arg310, Asp331 and Asn386 are conserved in coronaviruses, and their mutation to alanine in SARS-CoV has been shown to abolish N7-MTase activity[2,3,13]. Thus, although Asp331 is not involved in a direct hydrogen bond with the ligand, its interaction via a water molecule makes it crucial for N7-MTase activity[2,3]. Indeed, the entire nsp14 MTase-ligand interface is defined by an unusually large number of well-ordered water molecules that mediate hydrogen bonds between the ligand and the protein (Fig. 2a–c). Many of these are 'good waters' in that they bridge the MTase and SAM/SAH/SFG and can be considered as extensions of the MTase amino acids in the SAM/SAH/SFG binding pocket. Substitution of these water molecules will be an important feature to take into account in the design of SAM competitive inhibitors of the SARS-CoV-2 N7-MTase.

All the amino acids at the interface are conserved in the SARS-CoV nsp14 N7-MTase. The crystal structure of SARS-CoV nsp14/nsp10 with SAM captured a subset of the interactions (Extended Data Fig. 2), but some key interactions, such as between
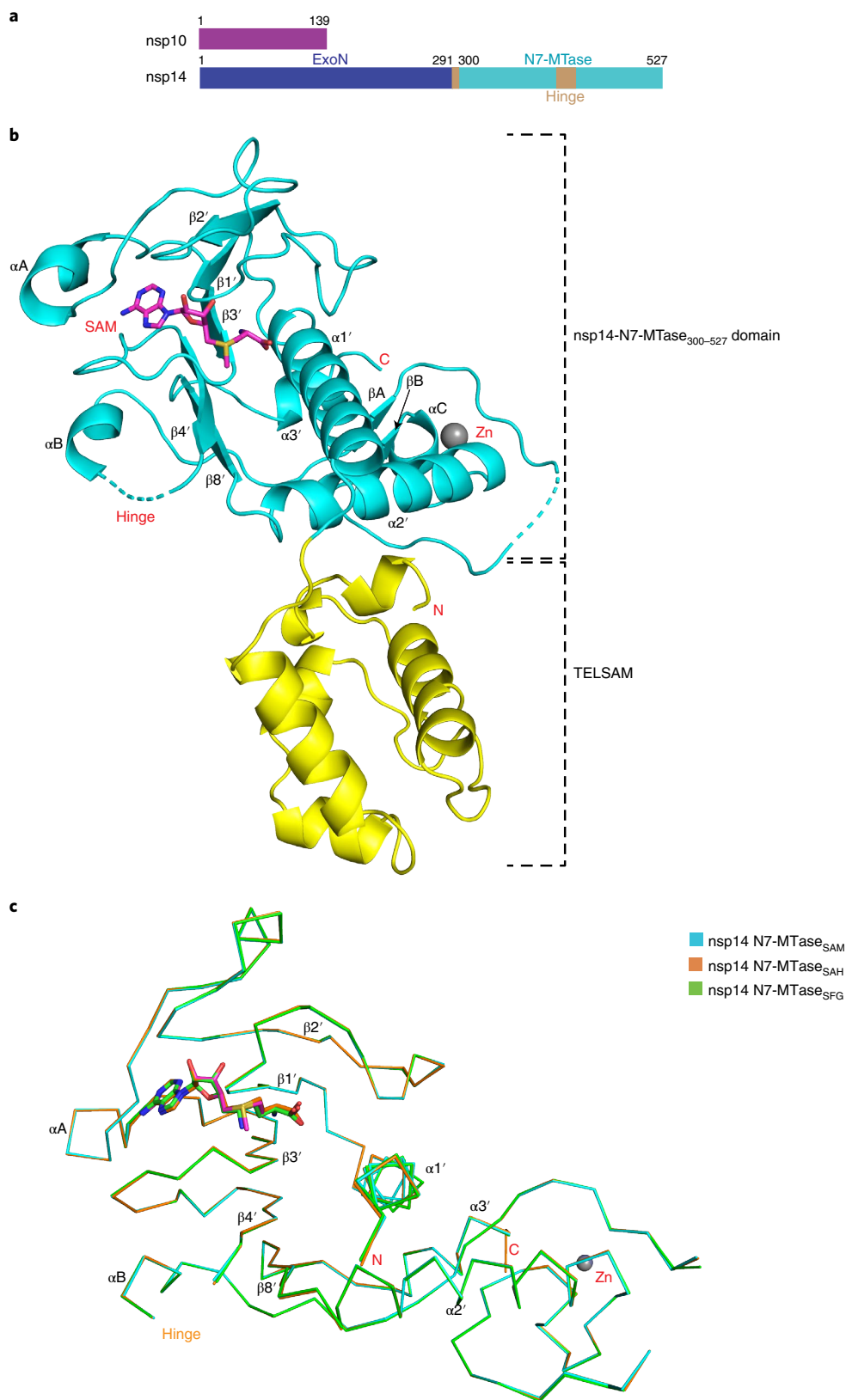
Fig. 1 | Overall structure of SARS-CoV-2 N7-MTase. a, Domain organization of SARS-CoV-2 nsp14 and nsp10. **b**, The overall structure of TELSAM-MTase fusion in complex with SAM shown in a ribbon representation. The nsp14 N7-MTase domain and TELSAM are colored in cyan and yellow, respectively. The secondary structure elements for the N7-MTase domain are labeled. The residues not modeled in the structure are shown by dashed lines. A zinc ion (Zn) is shown as a sphere and colored gray. **c**, C_α trace superposition of nsp14 N7-MTase$_{SAM}$, nsp14 N7-MTase$_{SAH}$ and nsp14 N7-MTase$_{SFG}$.
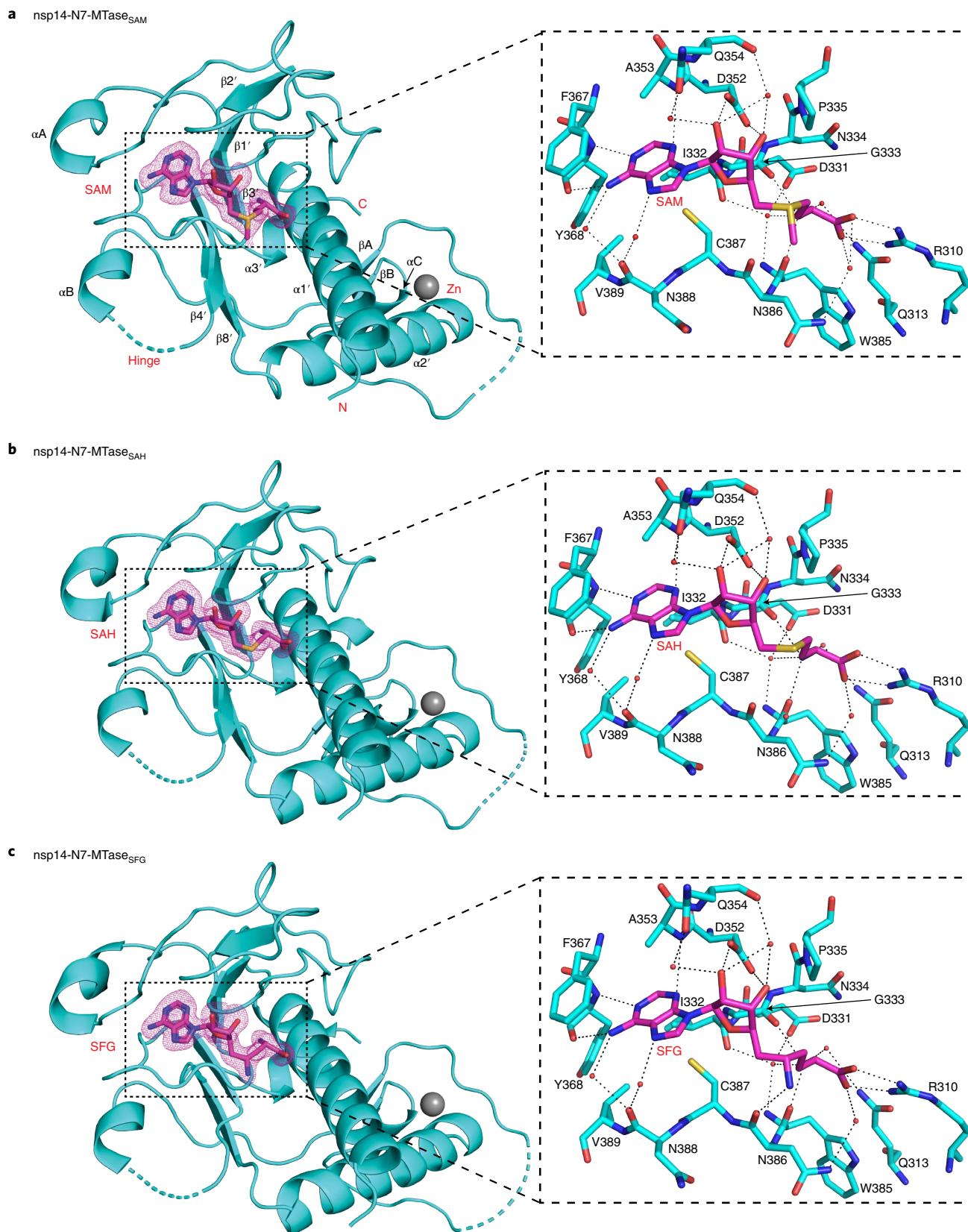
Fig. 2 | Details of SARS-CoV-2 nsp14 N7-MTase bound to ligands. a, Structure of nsp14 MTase domain bound to SAM (left), with a detailed view of the interactions between them (right). The $F_o - F_c$ difference electron density for SAM is shown in a pink mesh and contoured at 3σ level. Hydrogen bonds between the MTase domain and SAM are depicted as dashed lines and the water molecules are shown as red spheres. **b**, Structure of nsp14 MTase bound to SAH (left), with a detailed view of the interactions between them (right). **c**, Structure of nsp14 MTase domain bound to SFG (left), with a detailed view of the interactions between them (right).

Arg310, Gln313, Asn386 and the terminal carboxylate group of SAM were not observed, possibly because of the moderate resolution of the structure. Also, the configuration of the bound SAM is different, wherein the donor methyl group points in the opposite direction to what we observe here (Extended Data Fig. 2). Most importantly, the limited resolution of the SARS-CoV structure did not allow for the observation of water molecules, which form a crucial part of the N7-MTase-SAM interface (Extended Data Fig. 2).

Interestingly, because of the interconnection between the MTase domain and the ExoN domain (Extended Data Fig. 3), the MTase activity of the nsp14 is influenced by noncatalytic mutations in the ExoN domain[13–15]. To explore this further, we expressed and purified just the SARS-CoV-2 MTase domain (residues 289–527). We find that the MTase activity of the isolated MTase domain and the TEL-MTase fusion is nearly identical, showing that addition of TELSAM to the MTase domain does not impact its activity (Extended Data Fig. 4). But, consistent with the previous mutational and deletional analysis of SARS-CoV nsp14 (ref. [13–15]), the activity of MTase domain and the TEL-MTase is reduced in the absence of the ExoN domain (Extended Data Fig. 4). This is probably due to a stabilizing allosteric effect of one domain on the other, as mutations in the MTase domain have also been found to reciprocally effect the ExoN activity[3].

From isothermal titration calorimetry (ITC) analysis, SARS-CoV-2 nsp14/nsp10 complex binds SAM and SFG with similar affinities (K_d of 5.7 μM versus 4.4 μM), but binds SAH substantially better (K_d of 0.3 μM) (Supplementary Table 2 and Extended Data Fig. 5). The MTase domain and the TEL-MTase fusion bind SAM/SAH/SFG in a similar pattern, though the absolute affinities (K_d of around 22–25 μM for SAM/SFG and K_d of 5 μM for SAH) are lower than those observed with full-length nsp14/10 (Extended Data Fig. 6). This further reinforces the notion that the ExoN domain has a stabilizing allosteric effect on the MTase domain and helps to increase its affinity for SAM/SAH/SFG. Importantly, the residues that interact between the two domains are distant from the SAM/SAH/SFG binding site (Extended Data Fig. 3).

How to explain the higher affinity of SAH compared with SAM or SFG? In the nsp14 MTase$_{SAM}$ structure, the donor methyl group of SAM (attached to its Sδ atom) abuts the Asn386 main chain carbonyl and seems to displace a water molecule that would normally be coordinated to the main chain carbonyl (Fig. 2a). Indeed, in the nsp14 MTase$_{SAH}$ structure, we observe a well-ordered water molecule coordinated to the Asn386 main chain carbonyl at a position that would be incompatible with the methyl group of SAM (Fig. 2b). The entry of this water molecule may provide a partial explanation for the higher affinity of SAH relative to SAM, particularly the more favorable enthalpic contribution to binding (Supplementary Table 2 and Extended Data Fig. 5). It is less clear, however, why SAH would bind better than SFG. The amino group of SFG (attached to its Cδ) makes a direct hydrogen bond with the Asn386 main chain carbonyl and would seem to compensate for the loss of a water molecule (Fig. 2c). Whether this hydrogen bond is less favorable enthalpically than a coordinated water molecule to the Asn386 main chain carbonyl is uncertain at present.

An attractive feature of SARS-CoV-2 N7-MTase as a drug target is its high conservation of sequence across other coronaviruses and nearly total conservation of sequence across all the strains of SARS-CoV-2 (Extended Data Fig. 7a,b). Interestingly, we find that the affinity of SAH for nsp14 is substantively better than for SAM or SFG; positing SAH as the scaffold of choice for the design of more potent SAM competitors. Indeed, when Devkota et al. added a nitrile group to position 7 of the adenine base of SAH, it further improved its potency and binding (K_d of 0.05 μM)[6] and a bulky aromatic substituent at the same place led to single-digit nanomolar inhibitors[16]. Notably, the N7-MTase-SAM/SAH/SFG interface also contains a conserved cysteine (Cys387) at 3.9 Å and 4.6 Å from the N7 and N6 atoms of the adenine base, respectively (Fig. 2), allowing for a suitable 'warhead'

on the adenine base to make a covalent bond with the conserved cysteine. Such covalent inhibitors have been designed previously for other MTases[17], including one that forms a covalent bond with Cys449 in the active site of protein arginine methyltransferase 5 (PRMT5)[18].

Overall, the high-resolution structures of SARS-CoV-2 nsp14 N7-MTase presented here will aid in the development of new antivirals against SARS-CoV-2 and other pathogenic coronaviruses.

Online content

References

1. V'Kovski, P., Kratzel, A., Steiner, S., Stalder, H. & Thiel, V. Coronavirus biology and replication: implications for SARS-CoV-2. *Nat. Rev. Microbiol.* **19**, 155–170 (2021).
2. Ma, Y. et al. Structural basis and functional analysis of the SARS coronavirus nsp14-nsp10 complex. *Proc. Natl Acad. Sci. USA* **112**, 9436–9441 (2015).
3. Ogando, N. S. et al. Structure-function analysis of the nsp14 N7-guanine methyltransferase reveals an essential role in Betacoronavirus replication. *Proc. Natl Acad. Sci. USA* **118**, e2108709118 (2021).
4. Lin, S. et al. Crystal structure of SARS-CoV-2 nsp10 bound to nsp14-ExoN domain reveals an exoribonuclease with both structural and functional integrity. *Nucleic Acids Res.* **49**, 5382–5392 (2021).
5. & Gorgulla, C. A multi-pronged approach targeting SARS-CoV-2 proteins using ultra-large virtual screening. *iScience* **24**, 102021 (2021).
6. Devkota, K. et al. Probing the SAM binding site of SARS-CoV-2 Nsp14 in vitro using SAM competitive inhibitors guides developing selective bisubstrate inhibitors. *SLAS Discov.* **26**, 1200–1211 (2021).
7. Liu, C. et al. Structural basis of mismatch recognition by a SARS-CoV-2 proofreading enzyme. *Science* **373**, 1142–1146 (2021).
8. Yan, L. et al. Coupling of N7-methyltransferase and 3′-5′ exoribonuclease with SARS-CoV-2 polymerase reveals mechanisms for capping and proofreading. *Cell* **184**, 3474–3485 e11 (2021).
9. Nauli, S. et al. Polymer-driven crystallization. *Protein Sci.* **16**, 2542–2551 (2007).
10. Nawarathnage, S. et al. Crystals of TELSAM-target protein fusions that exhibit minimal crystal contacts and lack direct inter-TELSAM contacts. *Open Biol.* **12**, 210271 (2022).
11. Schubert, H. L., Blumenthal, R. M. & Cheng, X. Many paths to methyltransfer: a chronicle of convergence. *Trends Biochem. Sci.* **28**, 329–335 (2003).
12. Ferron, F. et al. Structural and molecular basis of mismatch correction and ribavirin excision from coronavirus RNA. *Proc. Natl Acad. Sci. USA* **115**, E162–E171 (2018).
13. Chen, Y. et al. Structure-function analysis of severe acute respiratory syndrome coronavirus RNA cap guanine-N7-methyltransferase. *J. Virol.* **87**, 6296–6305 (2013).
14. Jin, X. et al. Characterization of the guanine-N7 methyltransferase activity of coronavirus nsp14 on nucleotide GTP. *Virus Res.* **176**, 45–52 (2013).
15. Chen, Y. et al. Functional screen reveals SARS coronavirus nonstructural protein nsp14 as a novel cap N7 methyltransferase. *Proc. Natl Acad. Sci. USA* **106**, 3484–3489 (2009).
16. Otava, T. et al. The structure-based design of SARS-CoV-2 nsp14 methyltransferase ligands yields nanomolar inhibitors. *ACS Infect. Dis.* **7**, 2214–2220 (2021).
17. Ferreira de Freitas, R., Ivanochko, D. & Schapira, M. Methyltransferase inhibitors: competing with, or exploiting the bound cofactor. *Molecules* **24**, 4492 (2019).
18. Lin, H. et al. Discovery of potent and selective covalent protein arginine methyltransferase 5 (PRMT5) inhibitors. *ACS Med. Chem. Lett.* **10**, 1033–1038 (2019).

Methods

Protein expression and purification. *Full-length nsp14/10 complex.* For ITC binding studies, a single pRSFDuet-1 plasmid bearing both C-terminal 6×His-tagged full-length nsp14 (*Nde*I and *Xho*I) and nsp10 (*Nco*I and *Not*I) was transformed into *E. coli* BL21Gold(DE3) cells (Agilent). The cells were grown at 37 °C until the culture reached an optical density OD_{600} of around 0.5, after which the temperature was reduced to 30 °C and $ZnCl_2$ added at a final concentration of 20 μM. At an OD_{600} of around 0.8, the temperature was reduced to 15 °C and expression of the complex was induced by addition of 0.5 mM IPTG. The culture was incubated for 18 h at 180 r.p.m. The cells were harvested by centrifugation and resuspended in binding buffer (25 mM Tris pH 7.5, 250 mM NaCl, 10% glycerol, 0.01% IGEPAL, 25 mM imidazole, 10 μM $ZnCl_2$ and 10 mM 2-mercaptoethanol). The cells were lysed by sonication in the presence of EDTA-free Pierce Protease Inhibitor tablets (Thermo Fisher) and 1 mM PMSF, and the cell debris were clarified by centrifugation. The filtered supernatant was loaded onto a HisTrap HP affinity column (GE Healthcare). The column was washed with the binding buffer to remove the nonspecific proteins bound to the column and the desired complex was eluted using the binding buffer with 500 mM Imidazole. The fractions containing the nsp14/nsp10 complex were concentrated and further purified by size exclusion chromatography using a HiLoad 16/600 Superdex 200 (GE Healthcare) column, pre-equilibrated with 100 mM KH_2PO_4/K_2HPO_4 buffer pH 8.0, 100 mM KCl, 0.01% IGEPAL, 5 mM 2-mercaptoethanol and 10% glycerol. The fractions containing pure nsp14/nsp10 complex were concentrated and used for ITC without freezing.

MTase domain. pGEX-6p-1 plasmid containing N-terminal GST tagged MTase domain (residues 289–527) was transformed into the *E. coli* C41(DE3) cells. The cells were grown at 37 °C until the OD_{600} reached around 0.8 and then the temperature was reduced to 18 °C and 0.5 mM IPTG and 20 μM $ZnCl_2$ added. The cells were harvested 18 h postinduction and resuspended in a GST-binding buffer (25 mM Tris pH 7.5, 500 mM NaCl, 10% glycerol, 0.01% IGEPAL, 10 μM $ZnCl_2$ and 2 mM DTT). After sonication, the supernatant was incubated with Glutathione Sepharose 4B beads (GE Healthcare) and washed with the GST-binding buffer to remove the nonspecific proteins. PreScission Protease was then added to the column and incubated overnight at 4 °C. The released MTase domain was collected as flowthrough. The fractions containing pure MTase domain were combined and the protein was further subjected to size exclusion chromatography.

TEL-MTase. Our efforts to crystallize various constructs and mutants of the nsp14/nsp10 complex and the N7-MTase domain alone (with and without various expressions tags and protein fusions such as green fluorescent protein (GFP)) were unsuccessful. Reports on the fusion of TELSAM with target proteins to improve their crystallization[9,10] motivated us to fuse the nsp14 MTase domain (residues 300–527) with TELSAM (residues 47–124) with different linkers (A, PA and PAA) and we carried out expression and protein purification as follows. The pRSFDuet-1-smt3 plasmids containing N-terminal 6×His-SUMO-TELSAM-MTase (TEL-MTase) were transformed into *E. coli* BL21Gold (DE3) cells. The cells were grown at 37 °C until OD_{600} reached 0.8. The temperature was reduced to 15 °C and IPTG and $ZnCl_2$ added to final concentrations of 0.5 mM and 20 μM, respectively. The cells were harvested 18 h postinduction and resuspended in the binding buffer (25 mM Tris pH 7.5, 500 mM NaCl, 10% glycerol, 0.05% IGEPAL, 30 mM imidazole, 10 μM $ZnCl_2$ and 10 mM 2-mercaptoethanol) in the presence of EDTA-free Pierce Protease Inhibitor tablets (Thermo Fisher) and 1 mM PMSF. The cells were lysed by sonication and the filtered supernatant was loaded onto a HisTrap HP affinity column (GE Healthcare). The column was washed with the binding buffer containing 1 M NaCl to remove nonspecific proteins bound to the column. The column was then re-equilibrated with binding buffer and Ulp1-Protease was added to the column to cleave the 6×His-SUMO tag. The cleaved protein was eluted and the fractions containing the 1TEL-MTase fusion protein were diluted to a final concentration of 50 mM NaCl and loaded onto a 5 ml HiTrap Q HP anion-exchange column (GE Healthcare). The protein was eluted in the unbound fractions and was further purified by size exclusion chromatography on a HiLoad 16/600 Superdex 200 (GE Healthcare) column using 25 mM Tris pH 8.3, 200 mM KCl and 2 mM TCEP. All of the purified proteins were concentrated and stored at −80 °C. For ITC studies, the size exclusion buffer was 100 mM KH_2PO_4/K_2HPO_4 buffer pH 8.0, 100 mM KCl, 0.01% IGEPAL, 5 mM 2-mercaptoethanol and 10% glycerol.

MTase activity assays. The MTase activity was measured using the MTase-Glo Methyltransferase bioluminescence assay (Promega)[19] following the manufacturer's instructions. The reaction mix containing 20 mM Tris pH 8.0, 50 mM NaCl, 1 mM EDTA, 3 mM $MgCl_2$, 0.1 mg ml⁻¹ BSA, 1 mM DTT, 20 μM protein (nsp14/10, MTase domain or TEL-MTase), 20 μM SAM and 0.15 mM G(5′)ppp(5′)A RNA cap analog (NEB, S1406S) were incubated for 1 h at room temperature. The detection solution from the kit was then added, and the mixture was further incubated for 30 min at room temperature, before the addition of the developing solution. Luminescence was measured by using a TECAN infinite 200Pro microplate reader. The averages and the s.d. of three measurements were plotted as a histogram using Origin v.7.0.

Isothermal titration calorimetry. The titrations were performed on a Microcal ITC_{200} instrument at 25 °C with the standard 10 μcals s⁻¹ reference power and at 600 r.p.m. The ligand SAM/SAH/SFG was loaded in the syringe (400 μM) and titrated into 40 μM of nsp14/nsp10 complex in the cell. For the MTase domain and TEL-MTase, concentrations of the protein and the ligands were 60 μM and 600 μM, respectively. Care was taken to ensure buffer match for the ligand and proteins to eliminate heat production due to the buffer mismatch. The titrations consisted of 15 injections of 2.5 μl ligand solution at a rate of 0.5 μl s⁻¹ at 180 s time intervals. An initial injection of 0.4 μl was made and discarded during data analysis. The data were fit to a single binding site model using the Origin v.7.0 software, supplied by MicroCal. All the experiments were repeated twice and average value reported.

Crystallization and structure determination of TEL-MTase with ligands. Crystallization trials for all the constructs were carried out at 15 mg ml⁻¹ with fivefold molar excess of the ligand (SAM, SAH and SFG). Initial screens were set up with Oryx Nano (Douglas Instruments) at 20 °C using commercially available screens in a sitting drop format with 0.3 μl of protein mixed with equal volume of reservoir solution. Among the three fusion constructs, only the fusion construct with a PAA linker produced initial hits. Initial crystals were observed in solutions containing 15% reagent alcohol, 0.2 M lithium sulfate and 0.1 M sodium citrate pH 5.5 in 2 days. The crystals were further optimized by varying both concentration of the reagent alcohol and also the pH of the buffer in hanging drop format using 1 μl protein with 1 μl reservoir. The crystals were cryoprotected in a stepwise manner with reservoir solutions containing 5–30% glycerol and flash-cooled in liquid nitrogen. X-ray diffraction data were collected at the NSLS-II 17-ID-1 and 17-ID-2 beamlines at the Brookhaven National Laboratory under cryogenic conditions.

The diffraction data were processed using DIALS and AIMLESS in the CCP4 suite[20,21]. The experimental data showed significant anisotropy and an anisotropic correction was performed using the STARANISO server (https://staraniso.globalphasing.org/cgi-bin/staraniso.cgi) with a surface threshold of $I/\sigma(I) \geq 1.2$. The structure was solved by molecular replacement with Phaser-MR[22] using the MTase domain of SARS-CoV (PDB-5C8T[2]) and TELSAM domain from PDB-7N1O[10] as search models. Subsequent iterative manual building and refinement were performed using Coot and Phenix Refine, respectively[23,24]. Ligand restraint file for SFG was generated using eLBOW[25] from the PHENIX suite. All molecular graphic figures were prepared using PyMOL (Schrödinger LLC).

Reporting summary. Further information on research design is available in the Nature Research Reporting Summary linked to this article.

Data availability

Atomic coordinates and structure factors for TELSAM-MTase-SAM, TELSAM-MTase-SAH and TELSAM-MTase-SFG have been deposited in the Protein Data Bank under the accession codes of 7TW7, 7TW8 and 7TW9, respectively. Source data are provided with this paper.

References

19. Hsiao, K., Zegzouti, H. & Goueli, S. A. Methyltransferase-Glo: a universal, bioluminescent and homogenous assay for monitoring all classes of methyltransferases. *Epigenomics* **8**, 321–339 (2016).
20. Evans, P. R. & Murshudov, G. N. How good are my data and what is the resolution? *Acta Crystallogr. D Biol. Crystallogr.* **69**, 1204–1214 (2013).
21. Winter, G. et al. DIALS: implementation and evaluation of a new integration package. *Acta Crystallogr. D Struct. Biol.* **74**, 85–97 (2018).
22. McCoy, A. J. et al. Phaser crystallographic software. *J. Appl. Crystallogr.* **40**, 658–674 (2007).
23. Emsley, P. & Cowtan, K. Coot: model-building tools for molecular graphics. *Acta Crystallogr. D Biol. Crystallogr.* **60**, 2126–2132 (2004).
24. Adams, P. D. et al. PHENIX: a comprehensive Python-based system for macromolecular structure solution. *Acta Crystallogr. D Biol. Crystallogr.* **66**, 213–221 (2010).
25. Moriarty, N. W., Grosse-Kunstleve, R. W. & Adams, P. D. electronic Ligand Builder and Optimization Workbench (eLBOW): a tool for ligand coordinate and restraint generation. *Acta Crystallogr. D Biol. Crystallogr.* **65**, 1074–1080 (2009).

Author contributions

J.K. and A.K.A. designed the experiments. J.K. performed all of the experiments. O.R. assisted in X-ray data collection and methylation assays. R.Q.-F. assisted in

Competing interests

Additional information

a. SARS-CoV-2 N7-MTase
1.62Å (Crystal)

b. SARS-CoV-2 nsp14/nsp10 complex
2.5Å (Cryo-EM, PDB 7N0D)

c. SARS-CoV nsp14/nsp10 complex
3.33Å (Crystal, PDB 5C8S)

d.

Extended Data Fig. 1 | Structural comparison of nsp14-N7-MTases. a. Structure of SARS-CoV-2 nsp14-N7-MTase$_{SAM}$ complex. **b**. Cryo-EM structure of SARS-CoV-2 nsp14/nsp10 heterodimer (PDB:7N0D, chain H). **c**. Crystal structure of SARS-CoV nsp14/nsp10$_{GpppA:SAH}$ complex (PDB:5C8S, chain B). The nsp14 MTase core, ExoN domain, and the hinge region are colored cyan, slate blue and orange, respectively. The nsp10 subunit is colored purple. **d**. Cα trace superposition of the MTase domains of SARS-CoV-2 (cyan) and SARS-CoV (PDB: 5C8T, chain B, orange). The bound SAM is also shown.

a.

SARS-CoV-2 N7-MTase

SARS-CoV N7-MTase (PDB 5C8T) 3.2Å

b.
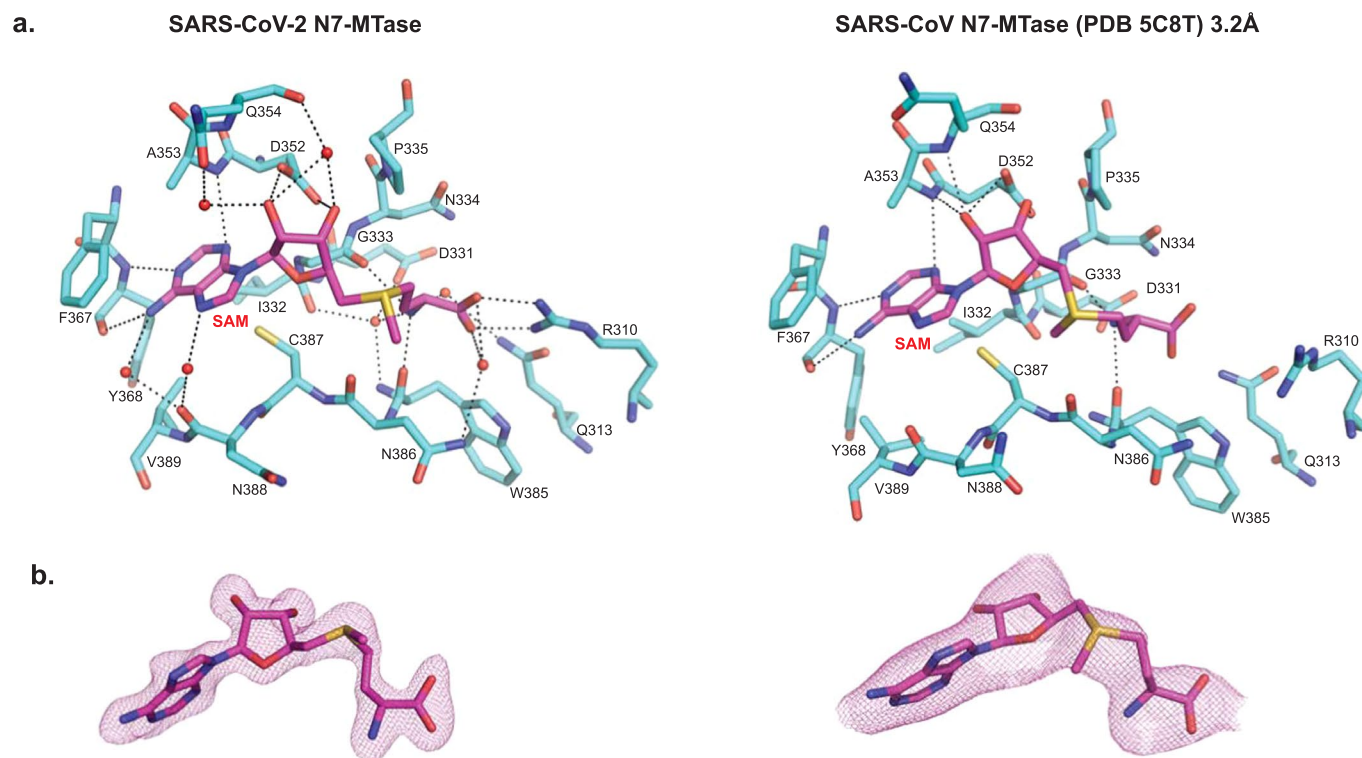
Extended Data Fig. 2 | Comparison of atomic binding details of nsp14-N7-MTase. a. Atomic binding details of SARS-CoV-2 nsp14-N7-MTase core (left) and previously reported SARS-CoV nsp14/nsp10 (PDB: 5C8T, chain B, right) with bound SAM. Hydrogen bonds are depicted as dashed lines and water molecules are shown as red spheres. **b**. Fo-Fc difference density map for SAM in the SARS-Cov-2 N7-MTase$_{SAM}$ (left) and SARS-CoV nsp14/10$_{SAM}$ structures (right) contoured at 3σ level.
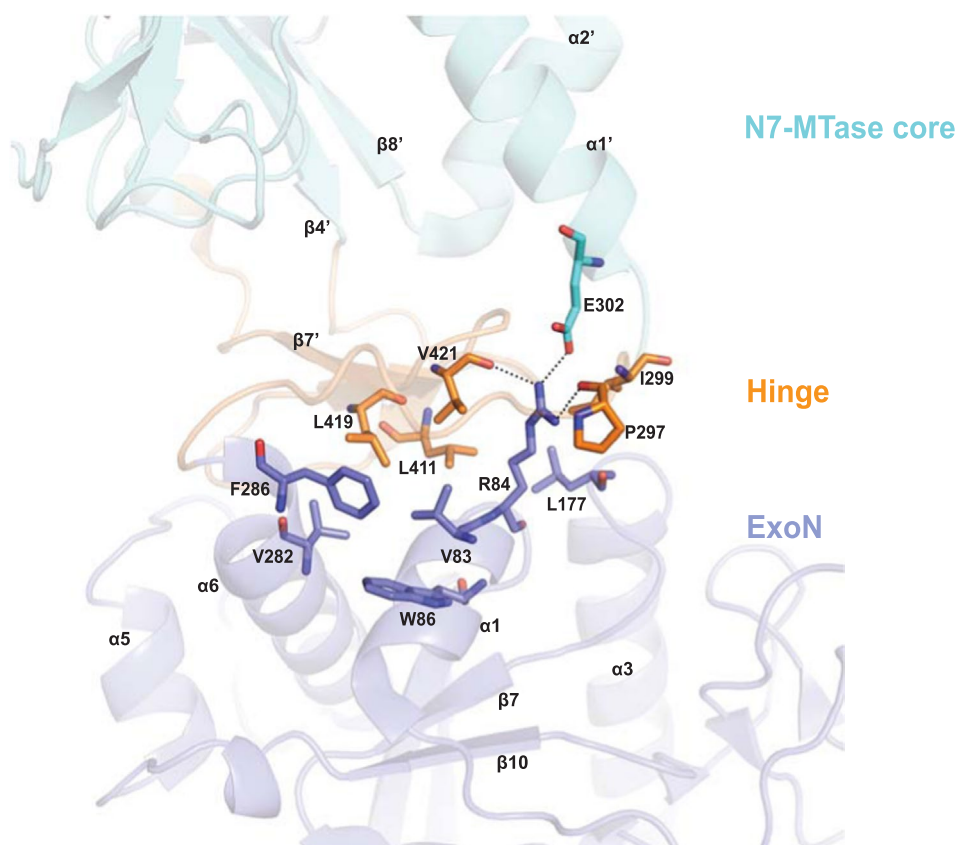
Extended Data Fig. 3 | Interactions between the MTase domain and ExoN domain. The nsp14 MTase core, ExoN domain, and the hinge region are colored cyan, slate blue and orange, respectively (PDB:7N0D). ExoN stabilizes the MTase domain via polar and non-polar interactions with the hinge and N7-MTase core.
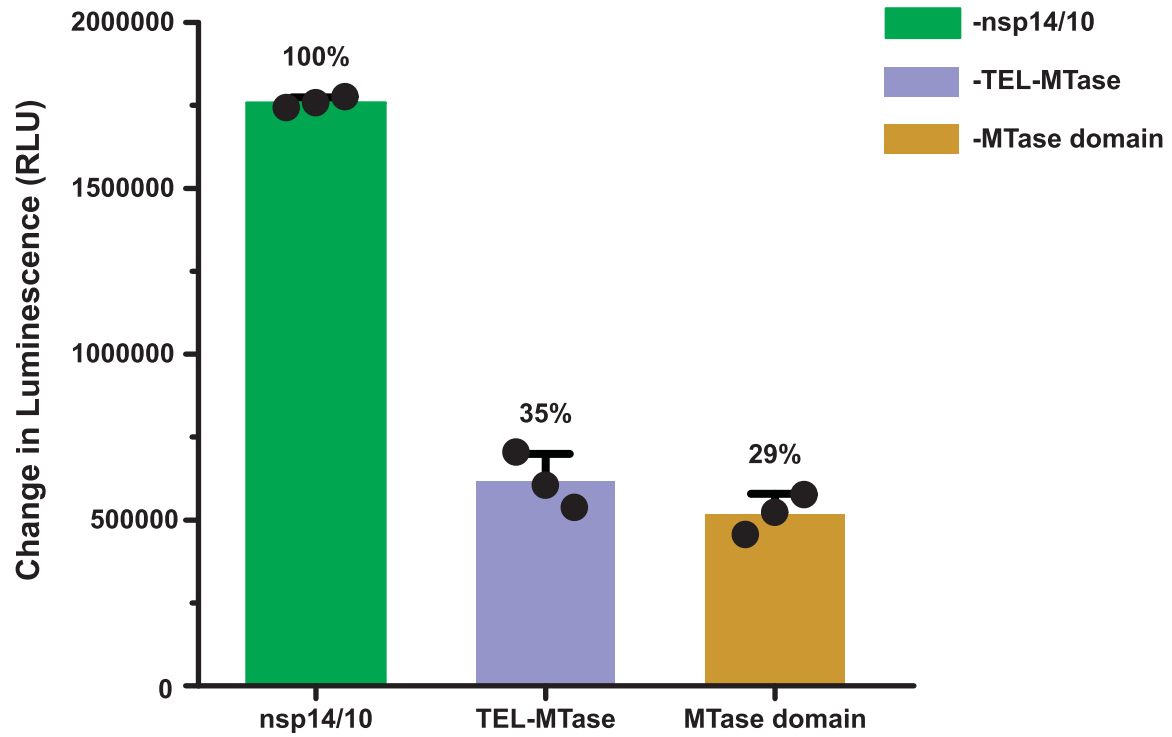
Extended Data Fig. 4 | Methyltransferase assay. The methyltransferase activity of the full length nsp14/10 complex compared with the TEL-MTase fusion and the MTase domain alone. Data represents the mean ± SD of three independent reactions.
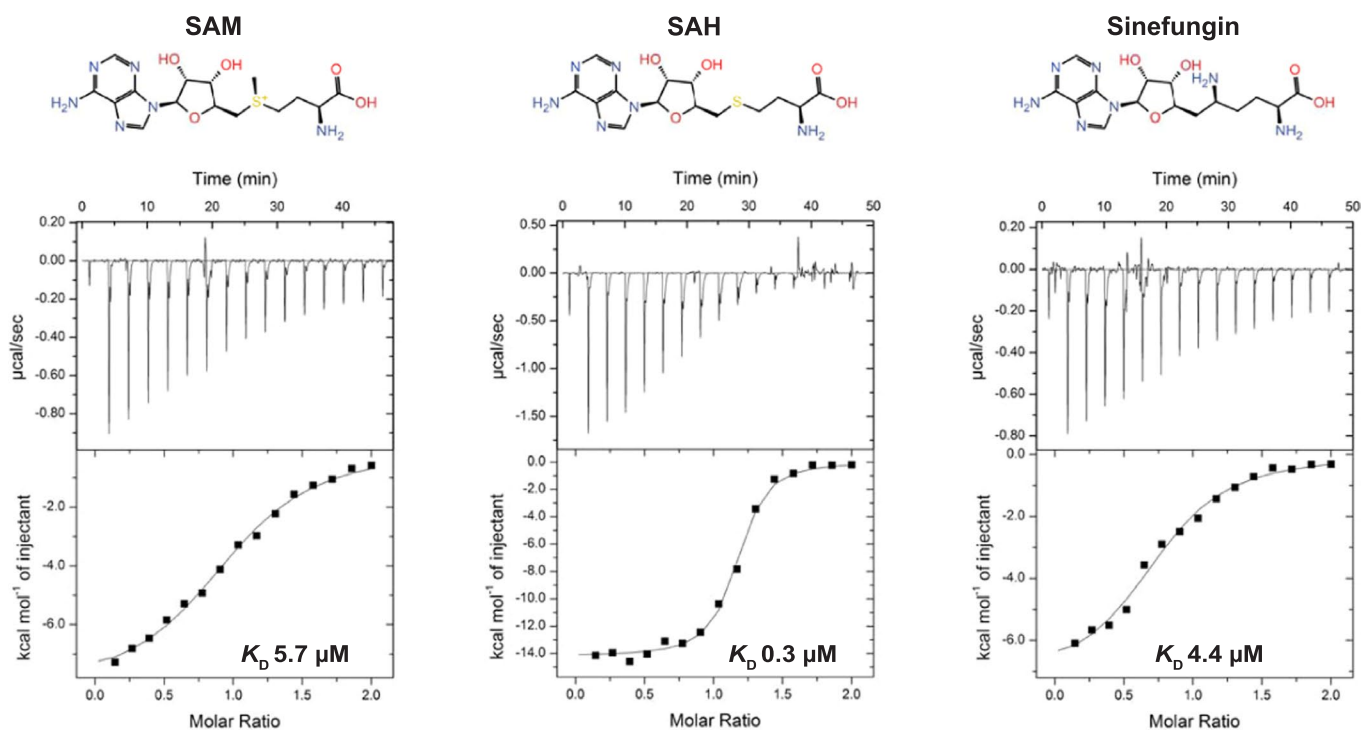
Extended Data Fig. 5 | ITC analysis of nsp14/10 complex with SAM, SAH and SFG. ITC titration data for SAM (left), SAH (middle) and SFG (right) with the nsp14/nsp10 complex are shown. The equilibrium dissociation constants (K_D) were derived from the resulting binding isotherms. The chemical structures of each ligand are also shown.

a.   **TEL-MTase**
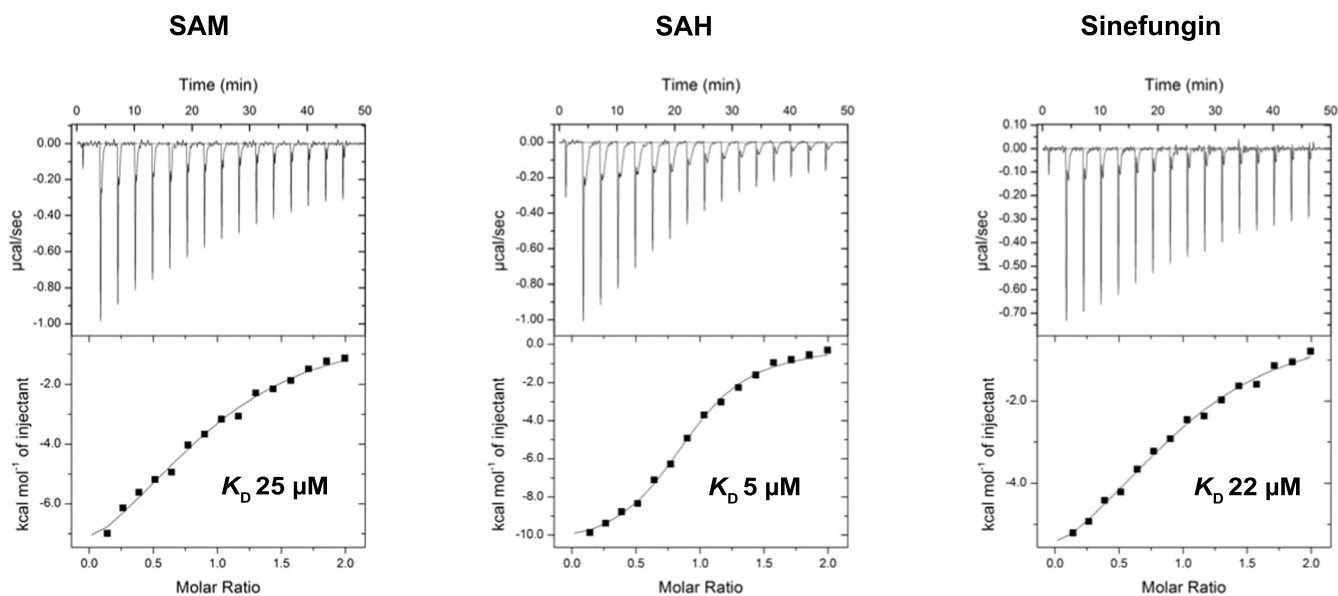
b.   **MTase domain**
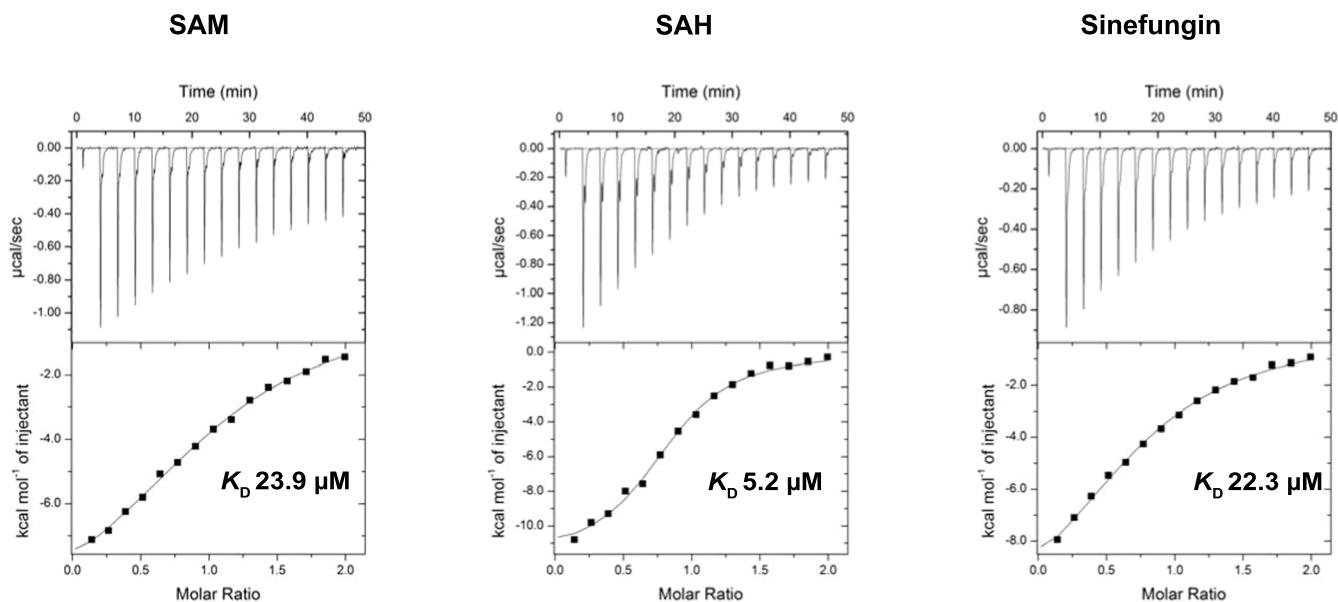
Extended Data Fig. 6 | ITC analysis of TEL-MTase and MTase domain with SAM, SAH and SFG. ITC titration data for SAM (left), SAH (middle) and SFG (right) with the TEL-MTase fusion (**a**) and the MTase domain alone (**b**). The equilibrium dissociation constants (K_D) were derived from the resulting binding isotherms.

a.

b.

Extended Data Fig. 7 | Sequence comparison. a. Sequence alignment of the nsp14 N7-MTase domain from 7 pathogenic coronaviruses. The identical and similar residues are highlighted in dark gray and light gray, respectively. **b**. Sequence alignment of the nsp14 N7-MTase domain of SARS-CoV-2 and its variants. The secondary structure elements are shown above the sequence alignment. Red triangles highlight residues that interact with SAM. Blue circles highlight residues that coordinate the zinc ion.

nature portfolio

Corresponding author(s): Aneel K. Aggarwal

Last updated by author(s): Jul 1, 2022

Reporting Summary

Nature Portfolio wishes to improve the reproducibility of the work that we publish. This form provides structure for consistency and transparency in reporting. For further information on Nature Portfolio policies, see our Editorial Policies and the Editorial Policy Checklist.

Statistics

For all statistical analyses, confirm that the following items are present in the figure legend, table legend, main text, or Methods section.

n/a	Confirmed	
☐	☒	The exact sample size (*n*) for each experimental group/condition, given as a discrete number and unit of measurement
☐	☒	A statement on whether measurements were taken from distinct samples or whether the same sample was measured repeatedly
☒	☐	The statistical test(s) used AND whether they are one- or two-sided *Only common tests should be described solely by name; describe more complex techniques in the Methods section.*
☒	☐	A description of all covariates tested
☒	☐	A description of any assumptions or corrections, such as tests of normality and adjustment for multiple comparisons
☒	☐	A full description of the statistical parameters including central tendency (e.g. means) or other basic estimates (e.g. regression coefficient) AND variation (e.g. standard deviation) or associated estimates of uncertainty (e.g. confidence intervals)
☒	☐	For null hypothesis testing, the test statistic (e.g. *F*, *t*, *r*) with confidence intervals, effect sizes, degrees of freedom and *P* value noted *Give P values as exact values whenever suitable.*
☒	☐	For Bayesian analysis, information on the choice of priors and Markov chain Monte Carlo settings
☒	☐	For hierarchical and complex designs, identification of the appropriate level for tests and full reporting of outcomes
☒	☐	Estimates of effect sizes (e.g. Cohen's *d*, Pearson's *r*), indicating how they were calculated

Our web collection on statistics for biologists contains articles on many of the points above.

Software and code

Policy information about availability of computer code

Data collection	X-ray diffraction data were collected at the NSLS-II 17-ID-1 and 17-ID-2 beamlines at the Brookhaven National Laboratory (BNL) under cryogenic conditions.
Data analysis	The diffraction data were processed using DIALS (version 2020.03.1) and AIMLESS (version 0.7.7) in the CCP4 suite version 7.1.018. The anisotropic correction was performed using the STARANISO server (https://staraniso.globalphasing.org/cgi-bin/staraniso.cgi) with a surface threshold of $I/\sigma(I) \geq 1.2$. The structure was solved by molecular replacement with Phaser-MR (Version 2.8.3). The structures were refined in Phenix refine (version 1.20rc3-4406) and the models were manually rebuilt in Coot (version 0.9.6 EL). Ligand restraint file for SFG was generated using eLBOW from the PHENIX suite ((version 1.20rc3-4406). All molecular graphic figures were prepared by PyMOL (Schrödinger LLC) version 2.4.0. Origin 7.0 software

For manuscripts utilizing custom algorithms or software that are central to the research but not yet described in published literature, software must be made available to editors and reviewers. We strongly encourage code deposition in a community repository (e.g. GitHub). See the Nature Portfolio guidelines for submitting code & software for further information.

Data

All manuscripts must include a data availability statement. This statement should provide the following information, where applicable:

- Accession codes, unique identifiers, or web links for publicly available datasets
- A description of any restrictions on data availability
- For clinical datasets or third party data, please ensure that the statement adheres to our policy

Atomic coordinates and structure factors for TELSAM-MTase-SAM, TELSAM-MTase-SAH and TELSAM-MTase-SFG have been deposited in the Protein Data Bank under the accession codes of 7TW7, 7TW8 and 7TW9, respectively. Source data for Extended Data Fig. 4 are available with the paper.

Field-specific reporting

Please select the one below that is the best fit for your research. If you are not sure, read the appropriate sections before making your selection.

☒ Life sciences ☐ Behavioural & social sciences ☐ Ecological, evolutionary & environmental sciences

For a reference copy of the document with all sections, see nature.com/documents/nr-reporting-summary-flat.pdf

Life sciences study design

All studies must disclose on these points even when the disclosure is negative.

Sample size	No Sample size calculation was required
Data exclusions	No data were excluded during the structure refinement using processed X-ray diffraction data sets.
Replication	For all the structures reported in this manuscript, data sets were collected from 3 to 5 different crystals. The single data set with best diffraction quality were used for further structure solution and refinement. In the ITC studies, the titrations were repeated twice and the average value is reported. The MTase assay were performed in triplicates. All replication attempts were successful and the data are shown in the corresponding figure. The source data for the MTase assay is provided.
Randomization	X-ray crystallography: Random assignment of reflections to working or free sets was automatically performed by Aimless program. Biochemical experiments: these experiments did not involve or require randomization.
Blinding	Data were not blinded, because subjective analyses were not applied to the structural and biochemical experiments described in this study.

Reporting for specific materials, systems and methods

We require information from authors about some types of materials, experimental systems and methods used in many studies. Here, indicate whether each material, system or method listed is relevant to your study. If you are not sure if a list item applies to your research, read the appropriate section before selecting a response.

Materials & experimental systems

n/a	Involved in the study
☒	☐ Antibodies
☒	☐ Eukaryotic cell lines
☒	☐ Palaeontology and archaeology
☒	☐ Animals and other organisms
☒	☐ Human research participants
☒	☐ Clinical data
☒	☐ Dual use research of concern

Methods

n/a	Involved in the study
☒	☐ ChIP-seq
☒	☐ Flow cytometry
☒	☐ MRI-based neuroimaging